CHEMISTRY OF MATERIALS

ARTICLE

pubs.acs.org/cm

In Situ Observation of Bimetallic Alloy Nanoparticle Formation and Growth Using High-Temperature XRD

Mehtap Oezaslan, Frédéric Hasché, and Peter Strasser*

The Electrochemical Energy, Catalysis, and Materials Science Laboratory, Department of Chemistry, Chemical Engineering Division, Technical University Berlin, Sekr. TC03, Strasse des 17. Juni 124, 10623 Berlin, Germany

Supporting Information

ABSTRACT: Bimetallic alloy nanoparticles exhibit a complex, (for the most part) poorly understood, crystallographic phase behavior, rarely following their macroscopic counterparts. We have studied formation kinetics, time scales of individual processes, compositional changes, and particle growth rates of Pt bimetallic alloy nanoparticles. We chose the Pt−Cu system, because of its technological importance as a precursor for core−shell nanoparticle electrocatalysts. We provide correlation of annealing control parameters, such as heating rate, temperature, and time, with microscopic alloy structure, composition, and particle size. We have clarified the roles of annealing temperature and time in the alloy formation process and traced out entire Vegard-type structure composition relationships over a wide temperature range. We have found that, during heating ramps, the annealing temperature essentially controls the Cu content of the resulting disordered Pt−Cu lattices. Increasing annealing times, in contrast, leads primarily to particle growth. Phase ordering occurs only during cooling. Our insight offers practical synthetic guidelines toward single-phase ordered and disordered $PtCu_3$ alloy nanoparticles with optimized particle dispersion.

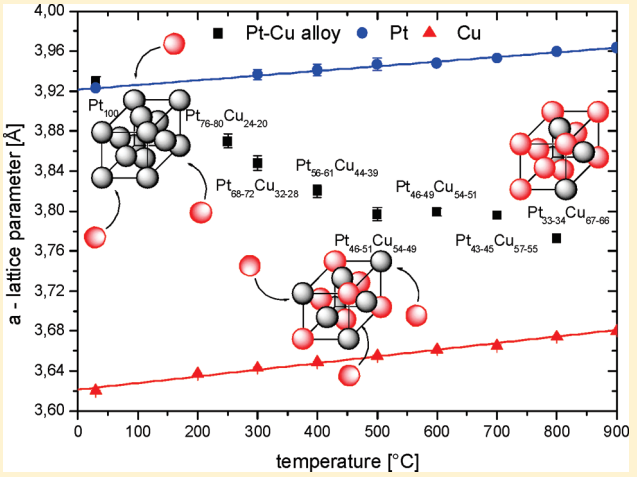

KEYWORDS: in situ high temperature XRD, $PtCu_3$, alloy formation, particle growth, phase transformation, bimetallic catalyst

1. INTRODUCTION

Bimetallic alloy nanoparticles have attracted considerable attention in many areas of science and technology, because their optical, magnetic, or catalytic properties differ significantly from those of their monometallic counterparts.[1] For instance, bimetallic nanoparticles often exhibit enhanced surface catalytic activity for different chemical reactions, which is attributed to the modifications in the surface electronic structure in combination with modified surface morphologies,[2−8] because of the atomic neighborhood of two dissimilar types of atoms. In polymer electrolyte membrane fuel cells (PEMFCs), pure platinum nanoparticles is the most widely used electrocatalyst for the oxygen reduction reaction (ORR), However, Pt-M bimetallic alloy nanoparticles (M = Fe, Co, Cu, Ni, etc.), in contrast, show greatly improved ORR activity at much reduced platinum costs.[9−19]

Electrocatalytic activity of bimetallic nanoparticles is critically sensitive to the structure, composition, and particle size of the alloy phases. The clarification of the structure−reactivity relationships of Pt-M alloy nanoparticle catalysts has been notoriously hampered by limited alloy crystal uniformity, because of the presence of multiple alloy phases (ordered, disordered, different compositions) in the thermally annealed catalyst materials.[16,20,21] Thermal annealing of bimetallic precursors is the most common synthetic step to form alloy nanoparticles,[22−25] yet rarely results in a pure alloy phase (in particular, for high molar ratios of M in Pt alloys).[20,26] Furthermore, macroscopic bulk alloys follow well-established thermodynamic phase diagrams, but alloys at the nanoscale do not typically ensue from those same structure−temperature relationships and phase stabilities.

Crystallographic phase uniformity of nanoparticle alloys was generally believed to improve, using sufficiently high annealing temperatures and extended annealing times, which, however, resulted in undesired large (>6 nm) nanoparticle diameters.[27] Virtually, all published Pt-M alloy particle preparations involving thermal treatment were optimized empirically without any detailed knowledge of the relationships between structural atomic parameters and annealing temperature and time. As a result of this, even the formation of single-phase Pt-M alloys with a desired nominal atomic ratio, with small (<6 nm, preferably <4 nm)

Received: December 23, 2010
Published: March 29, 2011

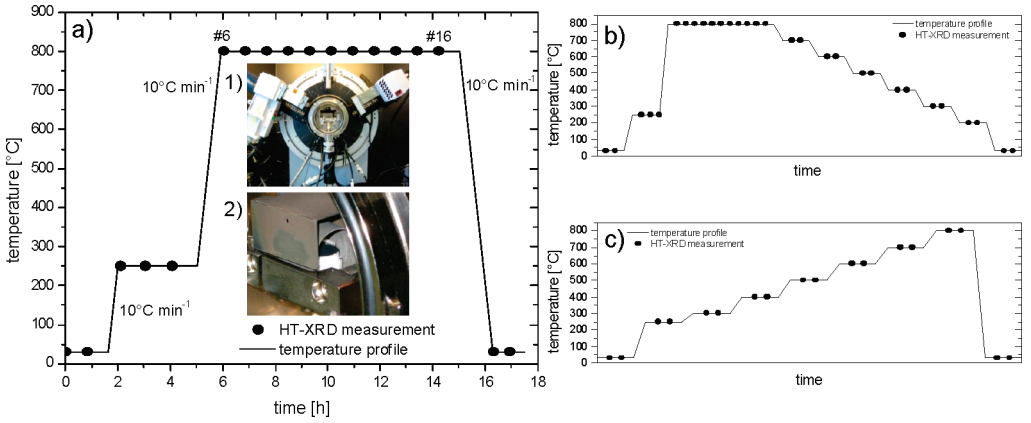

Figure 1. Temperature−time profiles used in this study to anneal Pt−Cu precursor materials in 4 vol % H_2/96 vol % Ar flux. Black circles indicate individual XRD measurements: (a) temperature−time program, referred to as a "synthesis protocol" ((1) top inset shows the assembly of HT-XRD with opened radiation heating chamber and (2) bottom inset shows the sample in a white Al_2O_3 crucible in the XRD furnace); (b) temperature−time program with constant temperature plateaus on the cooling ramp, referred to as a "stepped cooling protocol"; and (c) temperature−time program with constant temperature plateaus on the heating ramp, referred to as a "stepped heating protocol".

particle size and controlled lattice order has remained a major challenge.[24,28−30]

We study the thermal preparation of nanoparticle alloys with controlled properties and clarify the insight into the alloy formation dynamics. We report in situ measurements of the alloy formation process of bimetallic Pt−Cu alloy nanoparticles using high-temperature X-ray diffraction (HT-XRD). HT-XRD is a powerful technique to study in situ the formation of ordered or disordered crystallographic phases, combined with particle size. The Pt−Cu alloy system is of great technological interest, because single-phase $PtCu_3$ alloy nanoparticles serve as precursors for core−shell nanoparticle electrocatalysts with significantly improved activity for the electroreduction of oxygen in realistic fuel cells.[14,18,19,31−36] We correlate annealing temperature and annealing time with atomic lattice parameters, alloy phase composition, and particle size, and we clarify their role and relative time scales in the alloy formation process. In doing so, we map out entire Vegard-type structure−composition relations of the Pt−Cu nanoparticle system over a wide temperature range.

Our work gives atomic-scale insight in the phase formation behavior of a nanoscale bimetallic cubic Pt−Cu alloy system. We provide practical synthetic guidelines for the preparation of single-phase ordered and disordered bimetallic alloy nanoparticles.

2. EXPERIMENTAL SECTION

2.1. Preparation of Pt−Cu Precursor Materials. A Pt−Cu precursor material with a Pt:Cu ratio of 1:3 was formed using a Cu precursor impregnation onto a carbon-supported Pt nanoparticles followed by freeze drying. A commercial 28.2 wt % Pt nanoparticles supported on high-surface-area carbon (HSAC) (Part No. TEC10E30E, supplied by TKK, Japan) was mixed with an appropriate amount of $Cu(NO_3)_2 \cdot 2.5H_2O$ precursor (Sigma Aldrich, No. 467855 − 50 g) and deionized water. The suspension was then ultrasonicated for 15 min to produce a light viscous slurry. The black slurry was frozen in liquid nitrogen for 20 min and freeze-dried in vacuum (Labconco Freezone 6) for a few days. Finally, we obtained a dried, impregnated powder for the thermal annealing in a 4 vol % H_2/ 96 vol % Ar flux (100 mL min^{-1}).

2.2. In Situ High-Temperature X-ray Diffraction (HT-XRD) in Parallel Beam Geometry. Figure 1a−c shows the three annealing protocols (temperature−time profiles) for this study. The "synthesis protocol" (Figure 1a) represents a prototype of commonly used annealing protocols for the preparation of Pt bimetallic alloy nanoparticles in 4 vol % H_2/96 vol % Ar. This protocol included 2 h at 250 °C for precursor decomposition, followed by 9 h at maximum temperature for alloy formation and metal reduction with a heating rate of 10 K min^{-1}. After the cooling process with −10 °C min^{-1}, the reductive gas was switched to 1 vol % O_2/99 vol % N_2 at 30 °C for 2 h to prevent the carbon burning. Numerous in situ HT-XRD measurements in parallel beam geometry were conducted during the annealing protocol (noted by black circles along the temperature path in the figure). We used a D8 Advanced X-ray Diffractometer from Bruker AXS that was equipped with a Cu Kα source, a Goebel mirror, a position-sensitive LynxEye detector (PSD), and an external radiation heating chamber (supplied by MRI Physikalische Geraete GmbH, Germany). The inset of Figure 1 shows the HT-XRD setup with an opened radiation heating chamber on the goniometer. The heating assembly consists of an AlCr foil radiation heater, a rotated ceramic crucible as a sample holder, two gas lines and valves for a gas inlet/outlet, as well as a Kapton foil X-ray window against the radiation from the heater and sample at high temperatures.

Approximately 6 mg of Pt−Cu precursor material was placed in an alumina crucible and carefully flattened to form a smooth surface. The in situ XRD measurements in a parallel beam were conducted with the following parameters: step size, 0.04°; holding time, 3 s per step; fix divergence slit, 2 mm; and PSD Iris antiscattering slit setting, 13. A set of diffraction patterns was recorded every time in different 2Θ ranges (23.0°−25.0°, 33.5°−35.5°, and 36.5°−51.5°) from the beginning to the end of the experiment at a constant temperature. Black circles in Figure 1 indicate the individual XRD measurements.

To observe the modification change during the heating and cooling process, modified annealing temperature profiles were applied with temperature holds at intervals of 100 °C for 1.5 h between 800 °C and 200 °C/300 °C (see Figures 1b and 1c). The "stepped cooling protocol" exhibits temperature holds during the cooling ramp (−10 °C min^{-1}), while the "stepped heating protocol" shows temperature holds on the upward temperature ramp. These protocols served to establish the partial phase transformation from the disordered $PtCu_3$ alloy phase (space group $Fm\bar{3}m$) to the ordered $L1_2$ intermetallic crystal structure (space group $Pm\bar{3}m$). The final platinum loading of the annealed (fully decomposed) $PtCu_3$ sample was 22 wt %.

2.3. X-ray Diffraction (XRD) in Bragg−Brentano Geometry for Fine Resolution. High-resolution XRD spectra without the

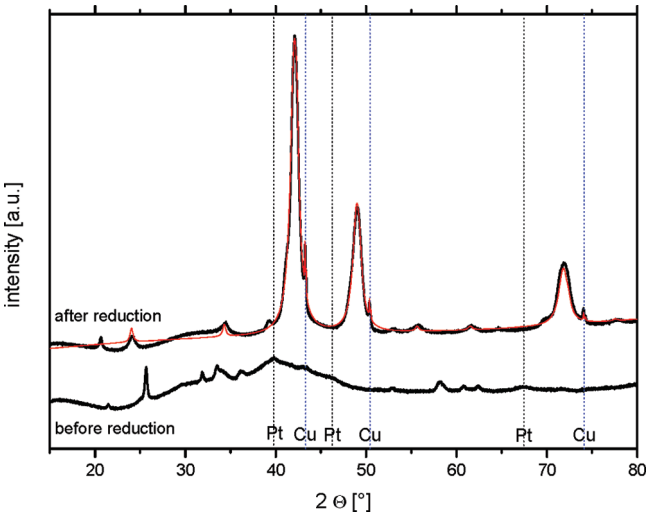

Figure 2. Room-temperature Bragg−Brentano geometry X-ray diffraction (XRD) patterns of carbon-supported $PtCu_3$ alloy nanoparticles before and after thermal annealing, according to the "synthesis protocol" of Figure 1a (denoted by black lines). A Rietveld refinement fit (denoted by the red line) served to determine the relative phase composition (R_{wp} = 4.10, R_{exp} = 0.60, GOF = 6.86). Vertical dotted lines denote bulk Pt and Cu reference patterns with $Fm\bar{3}m$ space groups.

additional reflections from the Al_2O_3 crucible were measured in a standard Bragg−Brentano geometry. We used a D8 Advanced X-ray Diffractometer equipped with a Cu Kα source, a position-sensitive LynxEye detector (PSD), and an automatic variable divergence aperture device. The following parameters were used: 2Θ range, 15°−80°; step size, 0.01°; holding time, 7 s per step; variable divergence slit, 4 mm; and PSD Iris antiscattering slit setting, 13; and sample rotation, 15 rpm.

2.4. XRD Profile Analysis and Rietveld Refinement for the Crystal Phase Quantification. All XRD diffraction patterns were analyzed using TOPAS (Bruker AXS, Version 4-2). The quantification of crystal phase structures was established by Rietveld refinement. The optimized parameters, used during the refinements, were background coefficients, displacement correction, peak shapes, and cell parameters. The residual values of the refinement, R-weighted pattern (R_{wp}), *R*-expected (R_{exp}), and goodness-of-fit (GOF) were evaluated. The stoichiometric composition of the crystal phase structure for Pt−Cu alloy was estimated using the Vegard's law. The Vegard's law describes the linear dependency on the lattice parameter of the alloy with those lattice parameters of the single components at the same temperature. The volume-averaged crystallite size was determined with the integral breadth method, which is independent of the distribution in size and shape.

3. RESULTS AND DISCUSSION

3.1. Alloy Formation and Size Dynamics of $PtCu_3$ during the "Synthesis Protocol". We performed in situ HT-XRD measurements to observe the $PtCu_3$ alloy formation process during the thermal treatment in a reductive atmosphere via the "synthesis protocol", referenced in Figure 1a. Before we discuss the time-resolved in situ data, we briefly present a commonly conducted structural before/after analysis of annealed $PtCu_3$ bimetallic nanoparticles at room temperature to highlight the additional insight in the alloy formation process provided by our study.

Figure 2 shows two room-temperature XRD profiles for Pt−Cu materials before and after thermal annealing and reduction, recorded in a typically focused Bragg−Brentano geometry.

The initial XRD pattern (bottom profile) shows broad characteristic (111), (200), and (220) reflections consistent with $Fm\bar{3}m$ face-centered cubic (fcc) crystal structure of pure Pt. We started with commercial, already-formed Pt nanoparticles and impregnated it with a Cu precursor salt. The initial average particle size of Pt nanoparticles is 2.3 ± 0.7 nm via TEM and is in agreement with the average crystallite size of 2.4 ± 0.2 nm obtained from XRD (see the Supporting Information).

Many small peaks are likely related to the crystalline copper nitrate precursor and cannot match those of pure metallic Cu. After the annealing, the XRD pattern for Pt−Cu alloy nanoparticles (top profile) revealed the presence of ($Fm\bar{3}m$) disordered alloy crystal phase, ($Pm\bar{3}m$) ordered intermetallic, and unalloyed ($Fm\bar{3}m$) pure Cu. The (111), (200), and (220) reflections of the disordered Pt−Cu alloy phase were shifted to higher 2Θ angles, with respect to pure Pt, consistent with a contraction of the lattice and alloy formation. The relatively sharp XRD peaks indicated a significant growth in size of particles after the thermal annealing. The ordered $L1_2$ $PtCu_3$ phase ($Pm\bar{3}m$) was recognized by superlattice reflections at 24.1°, 34.3°, 55.7°, and 61.5°, whereas the pure fcc Cu was found by very sharp XRD reflections at 43.3°, 50.4°, and 74.1°. Table 1 summarizes our results of crystal phases, space groups, lattice parameters, crystallite sizes, and Rietveld quantification of the sample.

The Rietveld analysis revealed that the disordered Pt−Cu alloy phase was the major component: ∼85.5 ± 2.5 wt %, with a crystallite size of 6.2 ± 0.2 nm. The minor fractions were the ordered $L1_2$ $PtCu_3$ (9.9 ± 2.0 wt %, 16.1 ± 1.8 nm) and the pure Cu (4.6 ± 1.1 wt %, with a very large particle size of ∼100 nm). The stoichiometric composition of the disordered fcc Pt−Cu phase was determined from the lattice parameter as $Pt_{28}Cu_{72}$ using Vegard's law, which is close to the nominal 1:3 ratio.[37]

The final XRD profile in Figure 2 highlights the major shortcoming of the Pt−Cu alloy preparation by the thermal annealing, in particular, the tradeoff between the alloy phase uniformity, composition, and crystallite size: one must choose between Pt-enriched alloy phases at a smaller particle size contaminated with nonalloyed residuals of metal M with a very-large-particle-size or uniform alloy phases with a controlled composition but unacceptably large particle size.

To obtain more-detailed and time-resolved insight into the processes during the annealing protocol, in Figure 3, we present a numbered series of in situ HT-XRD scans in parallel beam geometry of the Pt−Cu material, all taken at 800 °C over 9 h. Here, profiles 6−16 correspond directly to the circles and time instances in Figure 1a.

In Figure 3, the first experimental profile (#6) at 800 °C showed that the Pt−Cu alloy formation was, to a large extent, completed by the time the annealing temperature had reached 800 °C. We exclusively observed the formation of the single disordered fcc Pt−Cu alloy during the heating. The intensities of (111) and (200) reflections at 43° and 49.7° for unalloyed pure Cu (symbolized by "∧") gradually decreased, which indicated the continued Cu insertion in the Pt lattice and, simultaneously, a very slight positive 2Θ shift of Pt−Cu (111) and (200) reflections (symbolized by "*").

We analyzed the dynamics of the Cu insertion into the fcc alloy lattice and particle growth in more quantitative detail and present the evolution of lattice parameters, compositions, and

(crystallite) particle sizes during the annealing time at 800 °C in Figure 4. We used the Al_2O_3 reflections from the crucible as internal standards for all HT-XRD measurements to prove that the shift of reflections was affected by the temperature-dependent lattice expansion and alloy formation and not by displacement effects such as sintering and surface deformation. Lattice parameters of Pt and Cu cubic lattices, as a function of temperature, were established from HT-XRD reference profiles of carbon-supported Pt and Cu nanoparticles 3−4 nm in size at 800 °C in a reductive atmosphere. We assume that the experimental lattice parameters were the result of a balance between thermal lattice expansion effects and size-dependent lattice compression effects. The latter contribution, however, is likely to be small, because nanoparticles <2 nm in size show compressive lattice strain of up to a few percent, whereas the compressive lattice strain of particles 3−4 nm and beyond in size essentially vanishes.[38]

Table 1. Structural Investigation of Pt−Cu Alloy Nanoparticles after the Thermal Annealing

crystal phase	space group	Rietveld quantification [wt %]	crystallite size [nm]	lattice parameter [Å]
Cu	$Fm\bar{3}m$	4.6 ± 1.1	101 ± 30	3.6150 ± 0.0005
$PtCu_3$	$Fm\bar{3}m$	85.5 ± 2.5	6.2 ± 0.2	3.7150 ± 0.0005
$PtCu_3$	$Pm\bar{3}m$	9.9 ± 2.0	16.1 ± 1.8	3.6889 ± 0.0008

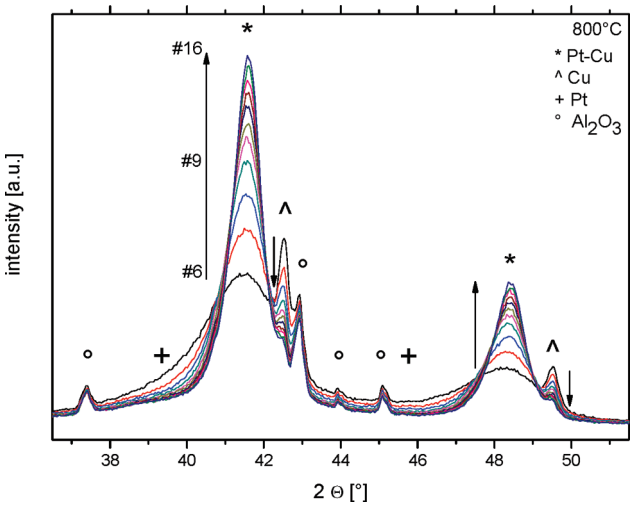

Figure 3. Series of XRD patterns, recorded in a parallel-beam XRD setup during Pt−Cu alloy formation at 800 °C over 9 h. Numbers indicate the first scan (#6, t = 0 h) and final (#16, t = 9 h) at 800 °C. Symbols denote individual crystallographic phases for disordered fcc Pt−Cu alloy, pure Cu, and Pt nanoparticles at 800 °C.

The average particle size was established from the (111) and (200) reflections of fcc Pt−Cu alloy, using an integral breath method (TOPAS 4-2). In Figure 4, two separate temporal regimes for the Cu insertion and particle growth are highlighted. The first regime (the "*Cu insertion regime*") was dominated by additional insertion of Cu atoms into the Pt alloy lattice in the first two hours at 800 °C. In this regime, composition changed from $Pt_{34-35}Cu_{66-65}$ to approximately $Pt_{29-30}Cu_{71-70}$, whereas the mean alloy particle size grew from 2.2 ± 0.4 nm to ∼3.8 ± 0.4 nm. Nevertheless, we noted that this additional amount of Cu was small, compared to that which had already been alloyed during the heating up to 800 °C. In the second regime (the "*particle growth regime*"), the changes in composition were negligible (from $Pt_{29-30}Cu_{71-70}$ to approximately $Pt_{28-29}Cu_{72-71}$); meanwhile, alloy particles grew dramatically from 3.8 ± 0.4 nm to almost 7.2 ± 0.5 nm after 9 h. The final average particles size is almost consistent with the result obtained from the highly resolved room-temperature XRD in Bragg−Brentano geometry.

Our results show that, during the heating ramp, the preferentially formed Cu-rich Pt alloy exhibits clearly a homogeneous disordered fcc phase structure, because of the absence of the superlattice reflections for an ordered $PtCu_3$ phase. We concluded that the annealing time principally controls the particle size and, therefore, should carefully be adjusted where highly dispersed nanoparticles are desired.

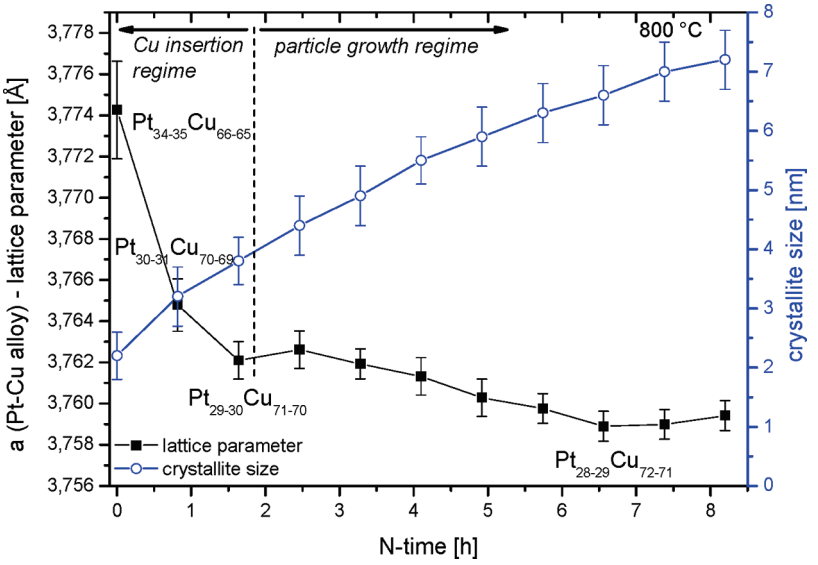

Figure 4. Lattice parameter of disordered Pt−Cu alloy and crystallite size versus normalized annealing time at 800 °C. The average crystallite size was determined from the (111) and (200) Pt−Cu reflections via integral breath method. The y-axis represents a, the lattice parameter; the x-axis represents the normalized annealing time, N-time (the value of 0 h represents the first scan (#6) at 800 °C in Figure 1a).

dx.doi.org/10.1021/cm103661q |*Chem. Mater.* 2011, 23, 2159–2165

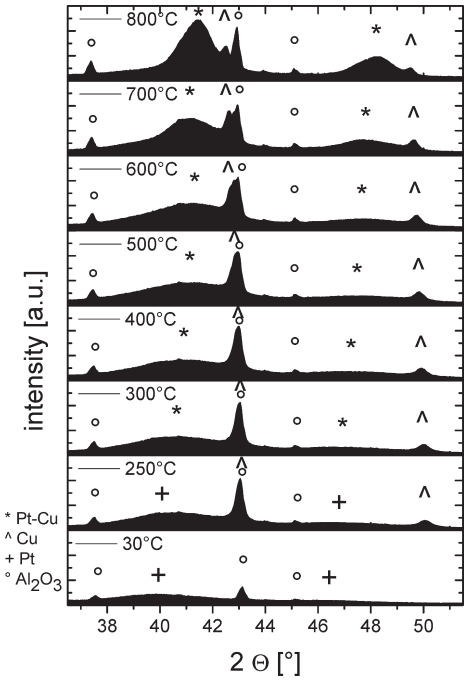

Figure 5. Series of in situ HT-XRD profiles, recorded in parallel beam XRD setup during the "stepped heating protocol" of Figure 1c. Disordered Pt−Cu alloy phase formation occurred at temperatures as low as 300 °C. Symbols indicate individual crystallographic phases.

The in situ study provides important practical implications for the synthesis of highly dispersed uniform alloy particles. Annealing protocols for $PtCu_3$ alloys with high dispersion (small particle size) can be kept much shorter, ca. 1−2 h than that often reported.[23,34,35,39−45]

3.2. Time-Resolved Formation of Disordered Alloys during the "Stepped Heating Protocol". The previous paragraph showed that, during the heating ramp, a major fraction of the non-noble-metal precursor was reduced and inserted as metallic Cu into the Pt lattice. We found moderate particle growth and preferred formation of the single disordered alloy phase over an ordered intermetallic compound. To obtain better insight into this dynamic alloy process, we recorded XRD profiles during modified heating ramps with each 90 min temperature hold in a reductive atmosphere ("stepped heating protocol" in Figure 1c). Figure 5 presents the series of in situ XRD scans taken at various constant temperatures.

It displays the dynamics of the alloy formation process, depending on temperature. The reduction of Cu ions to mostly metallic Cu particles was principally completed at temperatures below 300 °C. Thus, the formation rate of metallic Cu particles appears to be a fairly fast process, compared to the alloy formation or alloy particle growth. The Cu reflections shifted to smaller 2Θ values, based on the expansion of the cubic lattice. Again, we only observed the formation of the disordered crystal Pt−Cu alloy phase. Multiple crystal Pt−Cu phases, such as ordered phases, were not recorded in this experiment.

Using carbon-supported pure Pt and Cu nanoparticles, we performed calibration measurements and extracted the temperature-dependent lattice parameters of the pure metals and thereby established relative lattice parameter−composition relationships over a wide temperature range. This can be viewed as a family of Vegard's relations at elevated temperatures for nanoscale Pt−Cu alloys, as shown in Figure 6. A fairly linear lattice expansion with temperature was found for both pure metal nanoparticles at all temperatures, corroborating our earlier assumption that lattice contraction due to compressive strain is neglible at our mean particle diameters of 3−4 nm.[38]

The linear experimental dependence of the lattice and annealing temperature for supported pure fcc copper and platinum nanoparticles 3−4 nm in diameter is consistent with a constant expansion coefficient. The composition started at pure 100 at. % Pt at room temperature and decreased gradually in Pt to $Pt_{46-51}Cu_{54-49}$ at 500 °C. During the temperature holds of each 90 min, we observed only slight positive shifts of alloy reflections. This suggests that an almost-constant alloy composition was achieved within only minutes at any given temperature plateau. This leads us to the conclusion that the Cu insertion process into the Pt lattice is essentially controlled by temperature, not by annealing time.

The data in Figure 5 and the analysis in Figure 6 further reveal that the lattice parameters and alloy compositions changed gradually with annealing temperature up to ∼500 °C, beyond which they developed a plateau behavior. No effect on the obtained lattice parameter and alloy composition was observed again until a temperature of 800 °C was attained. It is unclear whether this is related to the order−disorder transitions of fcc Pt−Cu alloy phases.

Unlike that predicted in thermodynamic phase diagrams for macroscopic alloys, during the entire protocol at and below 600 °C, the thermodynamic stable ordered phase structure $L1_2$ was not detected. We hypothesize that a combination of kinetic effects and thermodynamic size effects may responsible for this. The diffusion coefficients of Cu and Pt lattice atoms may not be sufficient to mix enough Cu and Pt atoms over 90 min to form ordered phases; also, thermodynamic size and composition-dependent segregation effects of Cu, which favors surface segregation of Cu with increasing Cu content, may contribute and limit Cu alloying into the bulk of Pt particles.

3.3. Time-Resolved Formation of Ordered Alloys during the "Stepped Cooling Protocol". For more detailed information on the appearance of the ordered $PtCu_3$ phase, observed in the final XRD profile of Figure 2 in section 3.1, we directly followed the cooling process ("stepped cooling protocol"). Figure 7 shows the detected partial phase transformation from disordered fcc alloy to the thermodynamic stable ordered $L1_2$ $PtCu_3$ phase and their stability with the decrease of the temperature, derived from the superlattice peak reflection at ∼24° of the (100) lattice plane. The occurrence of this reflection reveals a reduction of the fcc unit cell symmetry with randomly distributed Cu and Pt atoms due to the ordered structure of Cu in the center of each face of the cube and of Pt in the edges. Other high 2Θ reflections, which indicated an ordered alloy, overlapped with reflections of disordered $PtCu_3$ alloy and Al_2O_3 materials.

The integrated intensity of the superlattice reflection grew slowly and directly reflects the rate of growth of the intermetallic $L1_2$ structure; however, we refrained from quantifying the ordered phase, because of the weak intensity of this reflection. Judged from the integrated intensities, prolonged annealing at 300−400 °C appeared to result in the largest ordered phase formation. The shift of the (100) superlattice reflection toward higher 2Θ values with lower temperatures was consistent with the thermally caused lattice contraction. Unlike our results on upward heating ramps, the formation of the ordered $PtCu_3$ phase at and below 600 °C is in agreement with the macroscopic bulk

dx.doi.org/10.1021/cm103661q |*Chem. Mater.* 2011, 23, 2159–2165

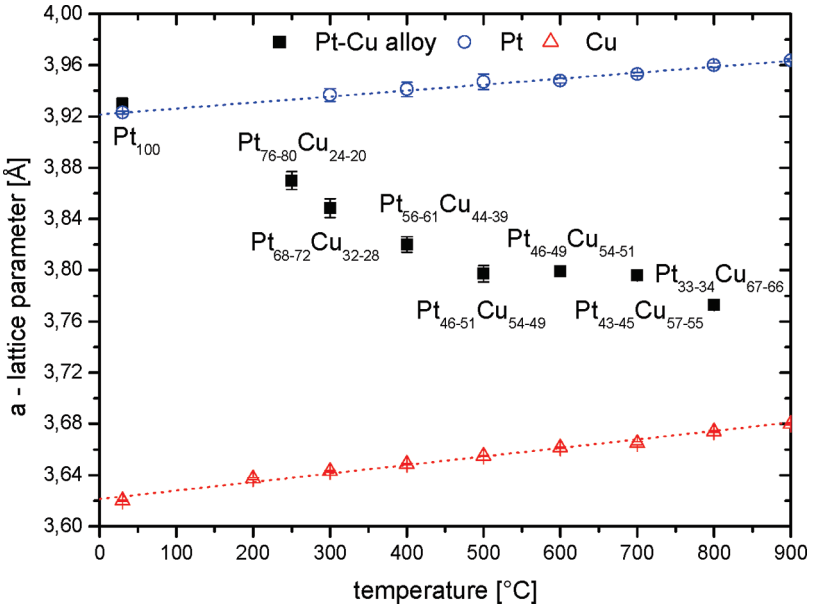

Figure 6. Lattice parameters and compositions of disordered Pt−Cu alloy nanoparticles at various temperatures (black squares Pt−Cu alloys, blue circles Pt, red triangles Cu) extracted from Figure 5. Composition was estimated using a temperature-corrected Vegard's rule.

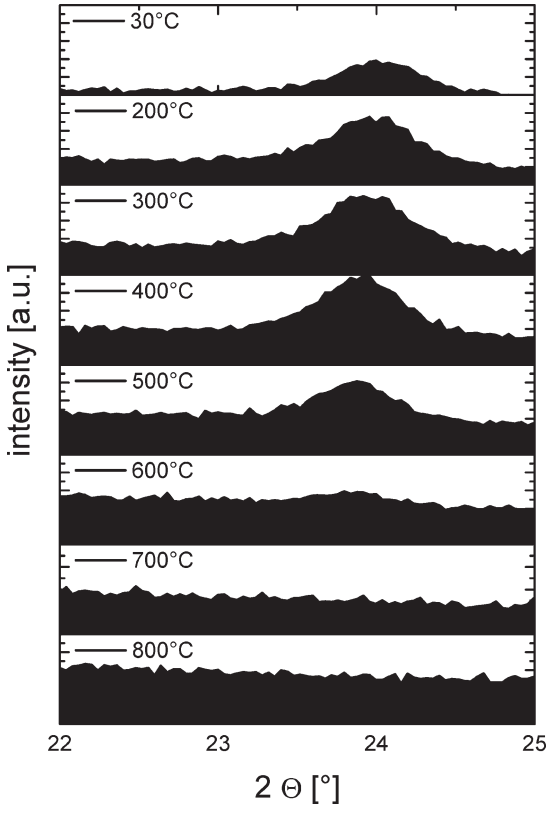

Figure 7. Series of in situ HT-XRD profiles, recorded in parallel beam XRD setup in the neighborhood of the (100) $PtCu_3$ superlattice reflection during the "stepped cooling protocol" of Figure 1b. Ordered $PtCu_3$ alloy phase formation occurred at temperatures below 600 °C.

alloy phase diagram. Nevertheless, the thermodynamic favorable ordered phase structure only amounted to ca. 10 wt % of the total material after the thermal treatment (Figure 2). The disordered $PtCu_3$ alloy phase was kinetically preferred and stabilized under our annealing conditions.

3.4. Electrochemical Activity for Oxygen Reduction. $PtCu_3$ alloy nanoparticles, prepared in the HT-XRD furnace, showed a significantly improved electrocatalytic activity for oxygen reduction. We used the rotating disk electrode (RDE) experiments in a deaerated 0.1 M $HClO_4$ electrolyte at room temperature (see Figure S1 in the Supporting Information) to measure the activity for ORR. Experimental details are given in the Supporting Information. In summary, the Pt mass based activity (A mg_{Pt}^{-1}) (see Figure S1d in the Supporting Information) of dealloyed $PtCu_3$ nanoparticle catalyst, annealed at 800 °C for 9 h, was 4−5 times higher than a benchmark Pt electrocatalyst, which was consistent with our earlier reports.[16,21,36,46]

4. CONCLUSION

We have studied the formation kinetics, time scales of individual processes, and particle growth rates of a Pt:Cu 1:3 bimetallic alloy, using in situ HT-XRD. We have clarified the roles of annealing temperature and time in the alloy formation process and traced out entire Vegard-type structure−composition relationships over a wide temperature range. Our results show the following:

- The maximum temperature during heating ramps largely determines the composition of the Pt−Cu alloy phase, that is, the extent of Cu insertion into a Pt lattice for bimetallic nanoparticles.
- Annealing time at constant temperature only results in minor additional Cu insertion for ∼1.5 h, which, however, causes sustained particle growth and therefore controls the particle size of the resulting alloy material. Annealing times can substantially be shortened without compromising composition.
- Cu reduction and formation of large pure Cu crystallites was more rapid than Pt alloy formation and particle growth, being essentially completed at merely 250 °C on the initial heating ramp.

dx.doi.org/10.1021/cm103661q |*Chem. Mater.* 2011, 23, 2159–2165

- Disordered $PtCu_3$ alloys are preferred during heating ramps, even at prolonged temperature holds.
- Ordered $PtCu_3$ structures only form on cooling ramps, with maximum order being achieved at ~400 °C.

Our work provides practical synthetic guidelines toward disordered or ordered highly dispersed $PtCu_3$ alloy catalysts.

■ ASSOCIATED CONTENT

Supporting Information. Electrochemical measurements of $PtCu_3$/HSAC, Pt/HSAC, and determination of the mean particle size for Pt/HSAC via TEM and XRD technique. This material is available free of charge via the Internet at http://pubs.acs.org.

■ AUTHOR INFORMATION

Corresponding Author

*Tel.: +49-30-314-29542. Fax: +49-30-314-22261. E-mail: pstrasser@tu-berlin.de.

■ ACKNOWLEDGMENT

The authors would like to thank Annette Wittebrock, Dr. Elisabeth Irran, MRI Physikalische Geraete GmbH, and Bruker AXS for their support and contributions. This project was supported by the Cluster of Excellence in Catalysis UNICAT, funded by the DFG and managed by the Technische Universität Berlin, Germany.

■ REFERENCES

(1) Cebollada, A.; Farrow, R. F. C.; Toney, M. F. . In *Magnetic Nanostructures*; Nalwa, H. S., Ed.; American Scientific: Stevenson Ranch, CA, 2002; pp 93−123.
(2) Stamenkovic, V. R.; Mun, B. S.; Mayrhofer, K. J. J.; Ross, P. N.; Markovic, N. M. *J. Am. Chem. Soc.* **2006**, *128* (27), 8702–8988.
(3) Zhang, J.; Mo, Y.; Vukmirovic, M.; Klie, R.; Sasaki, K.; Adzic, R. *J. Phys. Chem. B* **2004**, *108* (2004), 10955–10964.
(4) Stamenkovic, V.; Mun, B. S.; Arenz, M.; Mayerhofer, K. J. J.; Lucas, C. A.; Wang, G.; Ross, P. N.; Markovic, N. *Nat. Mater.* **2007**, *6*, 241.
(5) Zhang, J.; Lima, F. H. B.; Shao, M. H.; Sasaki, K.; Wang, J. X.; Hanson, J.; Adzic, R. R. *J. Phys. Chem. B* **2005**, *109*, 22701–22704.
(6) Chen, S.; Sheng, W.; Yabuuchi, N.; Ferreira, P. J.; Allard, L. F.; Shao-Horn, Y. *J. Phys. Chem. C* **2008**, *113* (3), 1109–1125.
(7) GreeleyJ; Stephens, I. E. L.; Bondarenko, A. S.; Johansson, T. P.; Hansen, H. A.; Jaramillo, T. F.; Rossmeisl, J.; Chorkendorff, I.; Norskov, J. K. *Nat. Chem.* **2009**, *1* (7), 552–556.
(8) Stamenkovic, V.; Moon, B. S.; Mayerhofer, K. J.; Ross, P. N.; Markovic, N.; Rossmeisl, J.; Greeley, J.; Norskov, J. K. *Angew. Chem., Int. Ed.* **2006**, *45*, 2897–2901.
(9) Gasteiger, H. A.; Markovic, N. M. *Science* **2009**, *324* (5923), 48–49.
(10) Stamenkovic, V. R.; Fowler, B.; Mun, B. S.; Wang, G.; Ross, P. N.; Lucas, C. A.; Markovic, N. M. *Science* **2007**, *315*, 493.
(11) Paulus, U. A.; Wokaun, A.; Scherer, G. G.; Schmidt, T. J.; Stamenkovic, V.; Radmilovic, V.; Markovic, N. M.; Ross, P. N. *J. Phys. Chem. B* **2002**, *106*, 4181–4191.
(12) Toda, T.; Igarashi, H.; Watanabe, M. *J. Electrochem. Soc.* **1998**, *145*, 4185.
(13) Chen, S.; Gasteiger, H. A.; Hayakawa, K.; Tada, T.; Shao-Horn, Y. *J. Electrochem. Soc.* **2010**, *157* (1), A82–A97.
(14) Strasser, P.; Koh, S.; Anniyev, T.; Greeley, J.; More, K.; Yu, C.; Liu, Z.; Kaya, S.; Nordlund, D.; Ogasawara, H.; Toney, M. F.; Nilsson, A. *Nat. Chem.* **2010**, *6*, 454–460.
(15) Liu, Z.; Yu, C.; Rusakova, I.; Huang, D.; Strasser, P. *Top. Catal.* **2008**, *49*, 241–250.
(16) Liu, Z.; Koh, S.; Yu, C.; Strasser, P. *J. Electrochem. Soc.* **2007**, *154* (11), B1192–B1199.
(17) Strasser, P.; Ata, M. *J. Phys. Chem. B* **1998**, *102*, 4131.
(18) Oezaslan, M.; Strasser, P. *J. Power Sources* In Press, Corrected Proof (DOI: 10.1016/j.powsour.2010.11.016).
(19) Oezaslan, M.; Hasche, F.; Strasser, P. *ECS Trans.* **2010**, *33*, (1), 333−341.
(20) Koh, S.; Yu, C.; Mani, P.; Srivastava, R.; Strasser, P. *J. Power Sources* **2007**, *172*, 50–56.
(21) Koh, S.; Strasser, P. *J. Am. Chem. Soc.* **2007**, *129*, 12624–12625.
(22) Schulenburg, H.; Müller, E.; Khelashvili, G.; Roser, T.; Bönnemann, H.; Wokaun, A.; Scherer, G. G. *J. Phys. Chem. C* **2009**, *113* (10), 4069–4077.
(23) Koh, S.; Hahn, N.; Yu, C.; Strasser, P. *J. Electrochem. Soc.* **2008**, *155*, B1281.
(24) Salgado, J. R. C.; Antolini, E.; Gonzalez, E. R. *J. Phys. Chem. B* **2004**, *108*, 17767–17774.
(25) Lima, F. H. B.; de Castro, J. F. R.; Santos, L. G. R. A.; Ticianelli, E. A. *J. Power Sources* **2009**, *190* (2), 293–300.
(26) Koh, S.; Toney, M. F.; Strasser, P. *Electrochim. Acta* **2007**, *52* (8), 2765–2774.
(27) Watanabe, M.; Tsurumi, K.; Mizukami, T.; Nakamura, T.; Stonehart, P. *J. Electrochem. Soc.* **1994**, *141* (10), 2659–2668.
(28) Koh, S.; Toney, M. F.; Strasser, P. *Electrochim. Acta* **2007**, *52*, 2765–2774.
(29) Antolini, E.; Cardellini, F. *J. Alloys Compd.* **2001**, *315* (1−2), 118–122.
(30) Hasche, F.; Oezaslan, M.; Strasser, P. *Phys. Chem. Chem. Phys.* **2010**, *12*, (46), 15251−15258.
(31) Mani, P.; Srivastava, R.; Strasser, P. *J. Power Sources* **2011**, *196*, 666−673.
(32) Strasser, P. *Rev. Chem. Eng.* **2009**, *25* (4), 255–295.
(33) Srivastava, R.; Mani, P.; Strasser, P. *J. Power Sources* **2009**, *190*, 40–47.
(34) Neyerlin, K. C.; Srivastava, R.; Yu, C.; Strasser, P. *J. Power Sources* **2009**, *186* (2), 261–267.
(35) Mani, P.; Srivastava, S.; Strasser, P. *J. Phys. Chem. C* **2008**, *112*, 2770–2778.
(36) Srivastava, R.; Mani, P.; Hahn, N.; Strasser, P. *Angew. Chem., Int. Ed.* **2007**, *46*, 8988–8991.
(37) Vegard, L. *Z. Phys.* **1921**, *5*, 2–26.
(38) Klimenkov, M.; Nepijko, S.; Kuhlenbeck, H.; Bäumer, M.; Schlögl, R.; Freund, H. J. *Surf. Sci.* **1997**, *391* (1−3), 27–36.
(39) Strasser, P.; Liu, Z.; Koh, S. *ECS Trans.* **2008**, *16* (2), 515–522.
(40) Koh, S.; Hahn, N.; Yu, C.; Strasser, P. *ECS Trans.* **2008**, *16* (2), 1093–1104.
(41) Tseng, C.-J.; Lo, S.-T.; Lo, S.-C.; Chu, P. P. *Mater. Chem. Phys.* **2006**, *100*, 385–390.
(42) Hoover, N. N.; Auten, B. J.; Chandler, B. D. *J. Phys. Chem. B* **2006**, *110*, 8606–8612.
(43) Serykh, A. I.; Tkachenko, O. P.; Borovkov, V. Y.; Kazansky, V. B.; Minachev, K. M.; Hippe, C.; Jaeger, N. I.; Schulz-Ekloff, G. *Phys. Chem. Chem. Phys.* **2000**, *2*, 2667–2672.
(44) Shapiro, E. S.; Takachenko, O. P.; Jaeger, N. I.; Schulz-Ekloff, F.; Grunert, W. *J. Phys. Chem. B* **1998**, *102*, 3798–3805.
(45) Obuchi, A.; Ogata, A.; Mizuno, K.; Ohi, A.; Ohuchi, H. *Physiochem. Eng. Aspects* **1993**, *80* (1993), 121.
(46) Strasser, P.; Koh, S.; Greeley, J. *Phys. Chem. Chem. Phys.* **2008**, *10*, 3670–3683.